Circular dichroism mode splitting and bounds to its enhancement with cavity-plasmon-polaritons

Research article

Denis G. Baranov*, Battulga Munkhbat, Nils Odebo Länk, Ruggero Verre, Mikael Käll and Timur Shegai

Circular dichroism mode splitting and bounds to its enhancement with cavity-plasmon-polaritons

https://doi.org/10.1515/nanoph-2019-0372
Received September 18, 2019; revised October 31, 2019; accepted November 1, 2019

Abstract: Geometrical chirality is a widespread phenomenon that has fundamental implications for discriminating enantiomers of biomolecules. In order to enhance the chiral response of the medium, it has been suggested to couple chiral molecules to resonant optical cavities in order to enhance the circular dichroism (CD) signal at the resonant frequency of the cavity. Here, we studied a distinctly different regime of chiral light-matter interaction, wherein the CD signal of a chiral medium splits into polaritonic modes by reaching the strong coupling regime with an optical microcavity. Specifically, we show that by strongly coupling chiral plasmonic nanoparticles to a non-chiral Fabry-Pérot microcavity one can imprint the mode splitting on the CD spectrum of the coupled system and thereby effectively shift the initial chiral resonance to a different energy. We first examined the effect with the use of analytical transfer-matrix method as well as numerical finite-difference time-domain (FDTD) simulations. Furthermore, we confirmed the validity of theoretical predictions in a proof-of-principle experiment involving chiral plasmonic nanoparticles coupled to a Fabry-Pérot microcavity.

Keywords: nanophotonics; strong coupling; chirality; polarization; plasmonics.

***Corresponding author: Denis G. Baranov,** Department of Physics, Chalmers University of Technology, 412 96 Göteborg, Sweden, e-mail: denisb@chalmers.se. https://orcid.org/0000-0002-8071-1587
Battulga Munkhbat, Nils Odebo Länk, Ruggero Verre, Mikael Käll and Timur Shegai: Department of Physics, Chalmers University of Technology, 412 96 Göteborg, Sweden

1 Introduction

An object is said to be chiral, if it cannot be superimposed with its mirror image by a sequence of rotations and displacements. The two mirrored versions in this case are called the left and right enantiomers. Geometrical chirality has fundamental implications on the electromagnetic response of chiral systems and materials. Any geometrically chiral absorptive object, being it a molecule or an optical nanoantenna, will exhibit circular dichroism (CD), that is, non-equal extinction of left and right circularly polarized (CP) light, in the absence of any magneto-optical activity [1, 2].

Geometrical chirality is ubiquitous in nature – it is encountered on many different length scales ranging from geometrical shapes of various living organisms to protein and DNA molecules. When acting on a biological receptor, opposite enantiomers of the same molecule may induce different response, such as odor or taste [3]. It is therefore important to have efficient ways of separating of different enantiomers of chiral biomolecules and detect their conformal changes [1, 4, 5]. This ability is even more pivotal for pharmaceutics, where the wrong enantiomer in a drug may be highly poisonous [6]. The phenomenon of CD provides an effective mean of optical discrimination between different enantiomers that otherwise look identical [7, 8]. An ability to enhance CD from chiral molecules is therefore of enormous importance to modern biotechnology.

Enhancement of light-matter interactions is typically achieved by using various kinds of optical cavities and resonators. It is therefore natural to expect that interfacing chiral molecules with such optical resonators would lead to an enhanced CD signal. Over the years, many attempts to realize these expectations have been made, including usage of Fabry-Pérot microcavities [9, 10], hotspots of plasmonic nanoantennas [11–17], and chiral metasurfaces producing superchiral light [7, 18]. The effect of the cavity leads to a local enhancement of optical chirality of incident light [19, 20] – a quantity determining the

degree of asymmetry between the interaction strengths of chiral light with left and right enantiomers [21, 22].

Here, we investigated an alternative interaction regime, wherein the optical cavity, instead of enhancing the chirality density of light, modifies and shifts the chiral response of a generic chiral scatterer, such as a chiral molecule or a chiral nanoparticle, to a different frequency region by virtue of strong coupling [23–25]. When the interaction rate of the material resonance with a cavity mode exceeds their corresponding decay rates, the system enters the strong coupling regime, characterized by the emergence of mode splitting and formation of intermixed light-matter eigenstates – polaritons. We have showed that not only transmission and absorption, but also the CD of a coupled system exhibits mode splitting in the strong coupling regime. At the same time, we have revealed fundamental limitations on the enhancement of the CD signal in planar resonators imposed by CP standing waves and suggest ways to overcome this limit. We have verified this effect with FDTD simulations and a proof-of-principle experiment utilizing chiral plasmonic nanoparticles as prototypical chiral scatterers interacting with a Fabry-Pérot microcavity.

2 Analytical calculations

The system under study is schematically presented in Figure 1 – it is formed by an array of chiral scatterers, such as chiral molecules, positioned inside a planar optical cavity. The chiral scatterers are expected to couple with the vacuum field of the Fabry-Pérot cavity mode, leading to the emergence of new hybrid eigenstates, which we refer to as cavity-polaritons, and giving rise to mode splitting in transmission and reflection spectra [26–28]. Due to the scatterers' inherent chirality, the system as a whole has to exhibit CD in the transmitted signal. Owing to the formation of polariton eigenstates, one may expect that not only transmission and reflection spectra, but also the CD spectra of the initial chiral system will also exhibit a similar mode splitting.

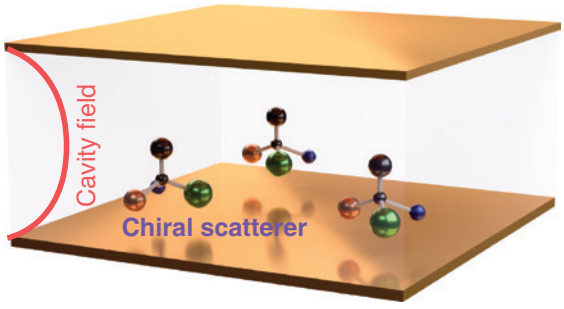

Figure 1: Sketch of the system under study: chiral scatterers are placed inside a planar cavity.

As a starting point of the analysis, we have modeled the chiral coupled system as a planar multilayer structure and calculated its optical response with the use of the transfer-matrix method (TMM, see Appendix A). The test structure consists of a bi-isotropic chiral layer placed between two gold mirrors that create a Fabry-Pérot cavity, as sketched in Figure 2A. The constitutive relations for a generic non-magnetic bi-isotropic material in SI units read [29] $\begin{pmatrix}\mathbf{D}\\ \mathbf{B}\end{pmatrix}=\begin{pmatrix}\varepsilon\varepsilon_0 & -i\kappa/c\\ i\kappa/c & \mu_0\end{pmatrix}\begin{pmatrix}\mathbf{E}\\ \mathbf{H}\end{pmatrix}$, where ε_0 and μ_0 are the vacuum permittivity and permeability, c is the speed of light, ε is the relative permittivity, and κ is the Pasteur parameter that couples the electric and magnetic fields. We modeled the chiral layer with the Lorentzian permittivity $\varepsilon=1+f_0\frac{\omega_0^2}{\omega_0^2-\omega^2-i\gamma\omega}$ and the corresponding dispersive Pasteur parameter $\kappa=\kappa_0\frac{\omega_0^2}{\omega_0^2-\omega^2-i\gamma\omega}$, where ω_0 is the resonance frequency of the chiral transition, γ is its linewidth, f_0 is the oscillator strength, and κ_0 is the amplitude of the Pasteur parameter [29].

Figure 2B shows transmission spectra of a bare cavity formed by two 20 nm thick gold mirrors as a function of the cavity thickness L, and that of a 20 nm thick bi-isotropic chiral layer in free space for $\omega_0=1.55$ eV, $\gamma=50$ meV, $f_0=0.5$, and $\kappa_0=0.03$. Owing to the Lorentzian dielectric response, the bi-isotropic layer is expected to strongly couple with the cavity mode and exhibit mode splitting in the transmitted signal. We then calculated CD spectra of the same chiral layer placed in the middle of the cavity as a function of the cavity thickness, Figure 2C. The calculated map of CD spectra clearly demonstrates anti-crossing between the two cavity-polariton modes. We note that we calculated CD as the difference in transmission between two different CP incident waves, T_+-T_- (where + and – refer to clockwise and counter-clockwise rotating electric field polarization). If a system is isotropic (or at least possesses $C_{3,z}$ rotational symmetry), it preserves circular polarization and the difference in reflection is zero due to reciprocity [30], thus the use of differential transmission and absorption is equivalent. If, however, it has at most $C_{2,z}$ symmetry, interpretation of both differential transmission and absorption becomes more complicated. To be consistent with further experiments, in which only transmission spectra were measured, we therefore used differential transmission T_+-T_- to quantify dichroic response.

Remarkably, the closer the polariton dispersion gets to the uncoupled chiral transition of the medium, the

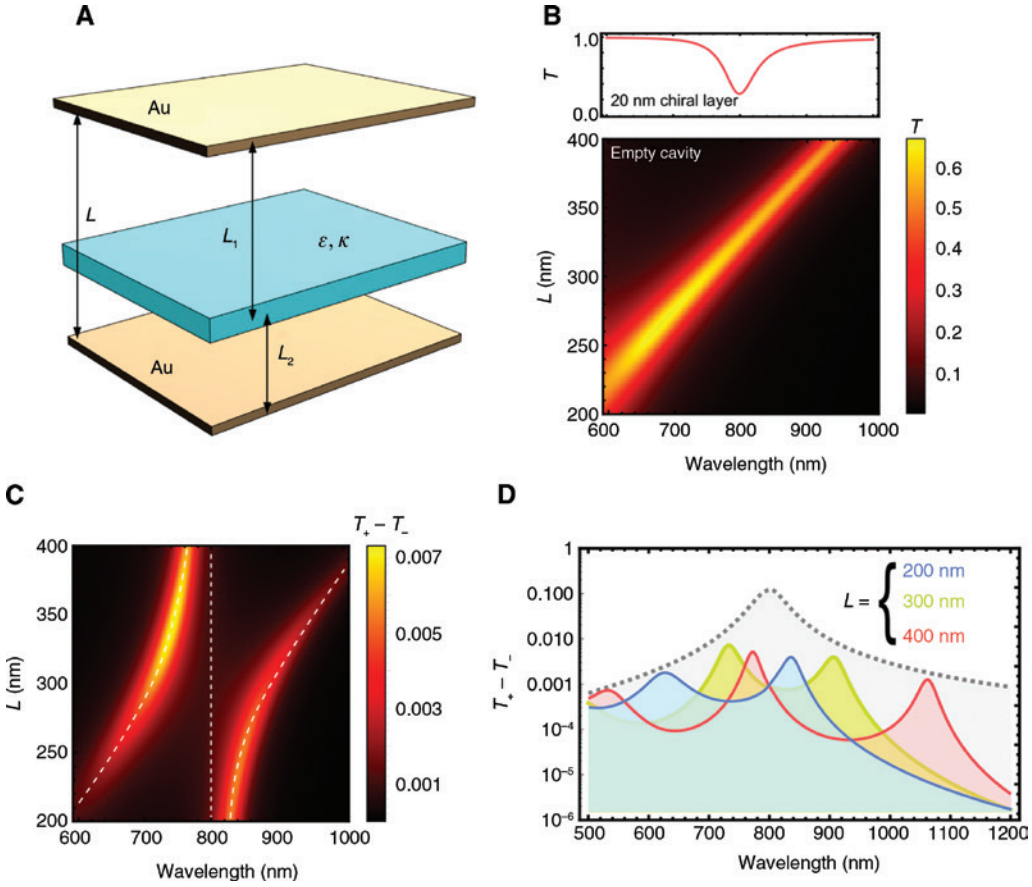

Figure 2: Transfer-matrix calculations of a chiral multilayer system.
(A) Sketch of the system studied with the TMM method: a bi-isotropic chiral layer characterized by a resonant permittivity ε and Pasteur parameter κ placed between two gold mirrors. (B) Transmission spectrum of a 20 nm thick bi-isotropic chiral layer in free space, and transmission spectra of an empty cavity as a function of its thickness. (C) CD spectra of the coupled system with the chiral film placed in the middle of the cavity as the function of the cavity thickness. (D) CD spectra of the 20 nm thick chiral film placed in the middle of the cavity of various thicknesses (solid curves) compared to that of the same film in vacuum (dashed grey). Note logarithmic scale in *y*-axis.

higher the CD magnitude is. This is an expected feature of the dispersion, since the composition of those polariton modes (in terms of the Hopfield coefficients) is dominated by the chiral material resonance, while strongly detuned polaritons have more cavity-like character. At the same time, for all thicknesses in Figure 2C the CD is strongly suppressed exactly at the wavelength of the material resonance, which is another manifestation of strong coupling.

When we compared these CD spectra to that of the bi-isotropic layer in vacuum, we found that CD from the layer in vacuum at all wavelengths exceeds that of the layer inside the cavity, Figure 2D. Noteworthy, such suppression of CD occurs despite enhanced electromagnetic field inside the cavity at the resonance, Figure 3A, and strong interaction between the cavity mode and the chiral layer manifested in the anti-crossing. The reason for this limitation becomes apparent when we look at the chirality density $C = -\frac{\varepsilon_0 \omega}{2}\mathrm{Im}(\mathbf{E}^* \cdot \mathbf{B})$ induced by an incident CP wave inside the cavity. As shown in Figure 3B, chirality density normalized by that of the incident CP wave at all wavelengths is less than unity. Since the asymmetry of light-matter interaction and CD magnitude is linked to the chirality density [22], CD produced by a chiral layer inside a planar Fabry-Pérot cavity, correspondingly, is also smaller than the free space value. In fact, this limitation of chirality density is fundamental to any isotropic passive planar cavity (i.e. without gain), and we discuss the origin of this limitation in the next paragraph.

Figure 3C illustrates the nature of this limitation: let us consider a CP wave of a certain handedness and carrying the corresponding chirality density $C_0 = -\frac{\varepsilon_0 \omega}{2}\mathrm{Im}(\mathbf{E}_0^* \cdot \mathbf{B}_0)$ and intensity $I_0 = \frac{1}{2}\mathrm{Re}(\mathbf{E}_0 \times \mathbf{H}_0)$ incident onto a planar

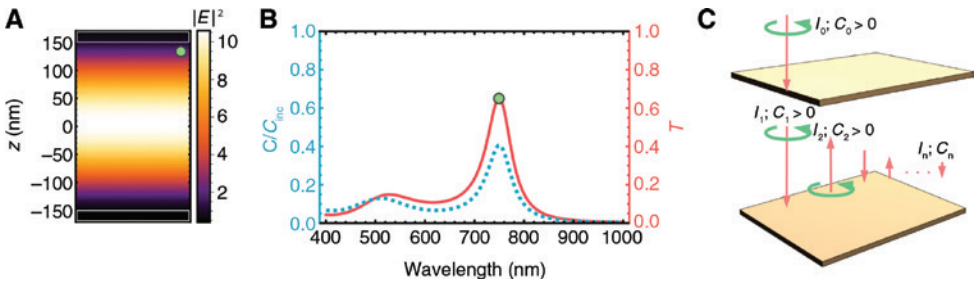

Figure 3: Limitation of optical chirality in planar isotropic cavities.
(A) Electric field enhancement inside an empty 300 nm thick cavity induced by a normally incident plane wave at a wavelength of 750 nm corresponding to the first order Fabry-Pérot resonance. (B) Spectrum of normalized chirality density C/C_{inc} induced by a normally incident CP wave inside a 300 nm thick Fabry-Pérot cavity formed by 20 nm thick Au mirrors. (C) Illustration of chirality density limitation inside isotropic planar cavities: an incident CP plane wave experiences a series of reflections inside the cavity, reversing its handedness each time.

cavity; let us assume for concreteness $C_0 > 0$. The cavity mirrors may have arbitrary composition; we will be interested in the empty cavity region between the mirrors where a chiral layer can be positioned later. As the wave experiences a series of reflections inside the cavity, the intensity I_i of each consecutive wave can only decrease. At the same time, the handedness of the travelling wave, which determines the sign of the chirality density, is reversed upon each reflection [29]. Furthermore, since C is a bi-linear function of fields, the chirality density of each consecutive wave in the empty region between the mirrors is $C_i = (-1)^{i-1}(I_i/I_0)C_0$. The total chirality density in this field distribution is

$$C = -\frac{\varepsilon_0 \omega}{2}\mathrm{Im}\left((\mathbf{E}_1 + \mathbf{E}_2 + \ldots + \mathbf{E}_i + \ldots)^* \cdot (\mathbf{B}_1 + \mathbf{B}_2 + \ldots + \mathbf{B}_i + \ldots) \right),$$

where $\mathbf{E}_i$ and $\mathbf{B}_i$ are the electric and magnetic field amplitudes of i-th CP wave. By direct calculations, one can easily verify that terms $\mathrm{Im}(\mathbf{E}_i^* \cdot \mathbf{B}_j + \mathbf{E}_j^* \cdot \mathbf{B}_i)$ vanish for $i \neq j$, so the total chirality density reduces to the sum of chirality densities of individual waves:

$$C = C_1 + C_2 + \ldots + C_i + \ldots.$$

This is a sign-alternating sum, such that $|C_{i+1}| < |C_i|$; therefore, it converges, and clearly $|C| < C_0$. This proves that the chirality density inside any planar passive isotropic cavity is smaller than that of the incident CP wave, which imposes bounds on the CD produced by a chiral layer placed inside a planar Fabry-Pérot cavity. Of course, this bound can be lifted by incorporating a gain medium, which would allow transmitted waves to have larger intensity and chirality densities. However, from the energy point of view it is equivalent to increase the incident CP wave intensity in a passive system.

Preserving the helicity of reflected waves is crucial to overcoming this fundamental limitation with planar structures [31]. A possible way to overcome the free space limit is to employ anisotropic mirrors with at most $C_{2,z}$ symmetry. Broken isotropy of the mirrors will allow to convert the polarization rotation direction upon reflection (clockwise to counter-clockwise and vice versa), thus preserving the sign of the chirality density of the travelling wave and enhancing the chirality density in the middle of the cavity [32]. Another recently suggested approach to bypass this limitation is based on oblique-propagating modes, which do not flip chirality upon reflection from specially designed metasurface mirrors [33]. Potentially, both of these approaches could allow obtaining enhanced CD and chiral mode splitting at the same time.

3 FDTD simulations: test of a real system

In order to test the analytical predictions, we performed a proof-of-principle experiment and the corresponding FDTD simulations with a coupled chiral nanoparticles-cavity system (see Appendix B for details of simulations). To ensure strong interaction of the chiral scatterer with the cavity, we have used chiral plasmonic nanocrescents [34–37] instead of molecules due to their large oscillator strength. Figure 4A shows the top, tilted, and side view of the nanocrescent model used in the simulations. They consist of a hemispheroid with 40 nm height and 65 nm in-plane diameter, connected to the "tail", which tapers down to 10 nm in height at the end; the outer diameter of the crescent is 150 nm. This shape is not only chiral, but is also highly anisotropic. We shall describe the effect of this anisotropy below.

Absorption cross-section spectra of a single Au nanocrescent in vacuum demonstrate two prominent peaks at ~600 and ~700 nm, respectively, Figure 4B (see Figure S1

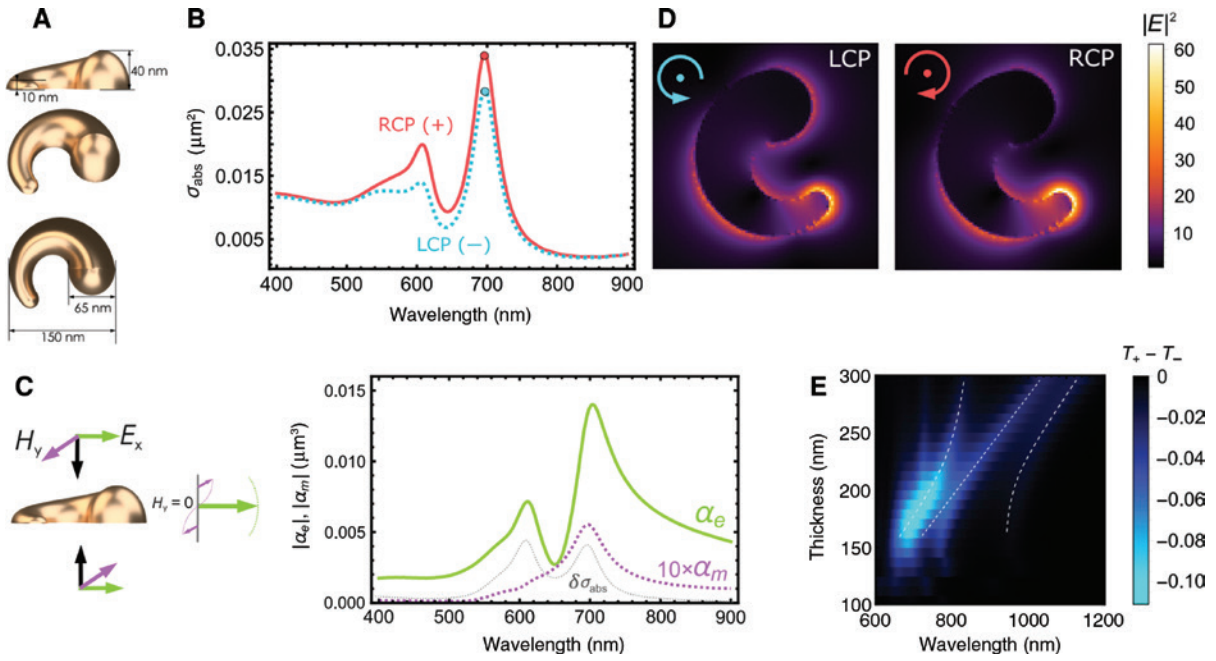

Figure 4: FDTD simulations of the chiral nanocrescent.
(A) Side, tilted, and top views of the Au nanocrescent model used in FDTD simulations rendered with the use of 3D software. (B) Simulated absorption cross-section spectra of a single Au nanocrescent in vacuum illuminated by a right- and left-circularly polarized plane wave from top. (C) Multipole decomposition of a single Au nanocrescent in vacuum placed in an electric field anti-node of a standing wave with *x*–polarized electric field (see inset). Solid curves depict the *x*–components of induced electric and magnetic dipoles, converted to electric and magneto-electric polarizability units (μm³) for convenient normalization; dashed curve shows the differential absorption cross-section $\sigma_{abs}^{RCP} - \sigma_{abs}^{LCP}$. (D) Simulated electric field intensity distributions excited by two circular polarizations in the horizontal plane at the base of a single Au nanocrescents in air. (E) Map of the simulated CD spectra of the coupled plasmon-cavity system versus the cavity thickness at normal incidence for a square nanocrescent array with 300 nm period placed in the middle of the PMMA-filled cavity. The dashed lines are guides for the eye.

for scattering and absorption cross-section spectra for two circular polarizations in the extended wavelength range); we have focused on the 700 nm resonance. Here and in the following, RCP/+ (LCP/−) refers to the polarization of light propagating in the negative *z*-direction with the *y*-component of the electric field being $\pi/2$ ahead (behind) of the *x*-component, corresponding to the complex electric field of $(1, \mp i)/\sqrt{2}$. Note that the differential absorption flips its sign around 850 nm (see Figure S1), indicating a change in sign of the magneto-electric cross-polarizability [22], which was studied by Goerlitzer et al. for a similar plasmonic nanocrescent structure and also demonstrated the CD sign flipping [37] (see Note S1 of Supporting Information for more discussion).

Optical chirality of our nanoparticle is further corroborated by multipole decomposition (see Appendix C) of a single nanocrescent placed in an electric anti-node of a linearly polarized standing wave, Figure 4C, which shows excitation of a magnetic dipole moment collinear with the induced electric dipole moment at the resonance wavelength of ~700 nm. The simulated electric field distributions in the horizontal plane excited by two circular polarizations at the 700 nm resonance reveal similar spatial distributions, Figure 4D, suggesting that the same eigenmode, but with different efficiencies, is excited with the two circular polarizations. Interestingly, this is in contrast to larger dielectric nanocrescents of the same shape, where excitation with opposite circular polarizations reveals quite different field distributions and more complex eigenmodes structure [34].

Next, we inspected the coupled plasmon-cavity system comprised by a square array of such nanocrescents with 300 nm period positioned in the middle of a Fabry-Pérot cavity formed by two 20 nm gold mirrors and filled with PMMA ($n = 1.45$). CD spectra at normal incidence calculated as a function of the cavity thickness expectedly exhibit the predicted mode anti-crossing, Figure 4E (note that the plasmon resonances of the nanocrescent redshift due to the dielectric around it). However, in addition to that, one can see a middle peak appearing in the CD spectra with almost linear dispersion following that of the empty cavity mode (see Figure S2), which is not predicted by the TMM

calculations. The same peak appears in the dispersion of transmission spectra under illumination with the two circular polarizations (see Figure S3). As one can infer from the separate transmission spectra, the magnitude of the mode splitting is nearly identical for both polarizations reaching around 390 meV for the 200 nm thick cavity. This splitting clearly exceeds $(\gamma_{pl}+\gamma_{cav})/2$ with $\gamma_{pl}\approx 120$ meV extracted from FDTD scattering spectra, and $\gamma_{cav}\approx 200$ meV taken from the calculated transmission spectra.

In order to unravel the origin of the middle peak in transmission and CD spectra, we must take the anisotropy of the nanocrescents into account. Non-equal total transmission, i.e. total intensity of transmitted light irrespective of its polarization state $T_+=|t_{++}|^2+|t_{+-}|^2$, $T_-=|t_{--}|^2+|t_{-+}|^2$ (where t_{ij} are the Jones transmission matrix elements in the basis of circular polarizations) of incident CP light through a planar structure, $T_+\neq T_-$, can often be misinterpreted as a manifestation of chirality, whereas the structure is in fact not chiral [38]. The lack of the three-fold rotational $C_{3,z}$ symmetry allows conversion between two circular polarized states ($t_{+-}\neq 0$, $t_{-+}\neq 0$) [38]. This polarization conversion is the source of non-equal total transmission $T_+\neq T_-$, which has nothing to do with chirality of the structure. In order to distinguish this so called elliptical dichroism from true circular dichroism, one needs to calculate complex-valued Jones matrix elements: non-equality $t_{++}\neq t_{--}$ will point out to chirality of the system. Calculated spectra of transmission Jones matrix elements for an array of nanocrescents in vacuum (see Figure S4) indicate that the observed response of Au nanocrescents originates from both their chirality and polarization conversion.

Polarization conversion is not the only consequence of the violated $C_{3,z}$ symmetry of the nanoparticles. We claimed that it also enables the middle peak in transmission and CD spectra of the coupled system. Eigenmodes of the Au nanocrescent participating in the coupling with the cavity modes have elliptical, rather than circular polarization due to its violated $C_{3,z}$ symmetry and induced generalized anisotropy [38]. Therefore, an incident circular polarization can be decomposed into the corresponding elliptical part, which will excite the coupled system and exhibit the mode splitting, and the remaining orthogonal part, which will not interact with the particles and show up in the transmission (or absorption) spectra close to the energy of the uncoupled cavity.

To substantiate this argument, we performed additional FDTD simulations that demonstrate the effect of violated $C_{3,z}$ symmetry. We simulated transmission through a square array of Au gammadions, which are characterized by $C_{4,z}$ rotational symmetry (so that the resulting array is characterized by the *p4* wallpaper symmetry group), placed in the middle of the cavity, and the same gammadions in which one central bar has been removed resulting in $C_{2,z}$ symmetry (with the array being characterized by the *p2* wallpaper group). $C_{4,z}$ symmetric particles possess circular eigenstates and thus preserve circular polarization; $C_{2,z}$ symmetric particles' eigenstates are, generally, elliptical. While $C_{4,z}$ symmetric particles exhibit a clear mode splitting and anti-crossing in transmission under illumination with CP light, Figure 5A, $C_{2,z}$ symmetric particles exhibit the bright middle peak in the transmission following the uncoupled cavity dispersion, Figure 5B. Correspondingly, the *p*4 symmetric array shows nearly zero differential transmission spectra T_+-T_- (with non-zero values attributed to the numerical errors of FDTD simulations), whereas the *p2* symmetric array clearly shows non-zero differential transmission caused by polarization conversion rather than chiral response (see Figure 5C,D). Note that both systems chosen for this demonstration are not geometrically chiral due to the preserved *xy*-plane mirror symmetry.

In order to verify that the predicted mode splitting in CD can exist without the uncoupled cavity resonance, we performed FDTD simulations with a chiral system possessing $C_{4,z}$ symmetry. We chose an array of horizontal metallic helices with its unit cell consisting of four identical helices rotated by 0, 90, 180, and 270° in order to maintain $C_{4,z}$ symmetry of the unit cell. The resulting CD spectra show a clear mode splitting without the uncoupled cavity peak, Figure S5.

4 Experiment

Lastly, we carried out a proof-of-principle experiment to confirm the prediction of mode splitting in CD of a chiral strongly coupled system. To that end, we have fabricated chiral gold nanocrescents using hole-mask colloidal lithography using techniques described in [34, 36] (see Appendix D for further details). Figure 6A shows SEM image of the fabricated gold nanocrescents on glass substrate, which indicates that the nanocrescents are distributed rather homogeneously over the large area (see Figure S6). Unpolarized transmission spectra through bare particles on glass substrate were then measured (see Appendix E for further details), revealing a broad transmission dip around 800 nm, see Figure 6B. This broad dip can be attributed to overlapping resonances of particles with varying sizes and/or aspect ratios, resulting in a shift of the plasmon resonance. Correspondingly,

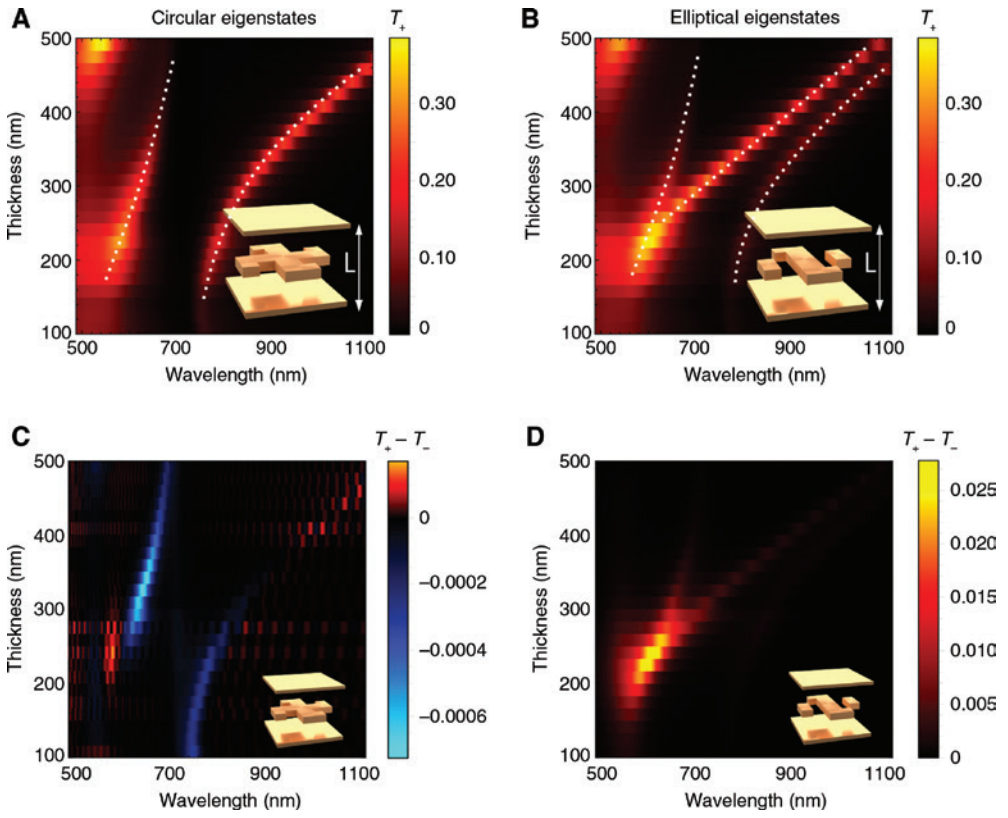

Figure 5: Effect of particle anisotropy on the mode splitting and anti-crossing under illumination with circularly polarized light.
(A) Transmission spectra through an array of Au gammadions with 125 nm period placed inside the middle of an empty Fabry-Pérot cavity formed by two 20 nm thick Au mirrors as a function of the cavity thickness. Dashed lines are guides for the eye marking approximate dispersion of polariton modes. (B) The same as (A) but for an array of gammadions with removed central bar. (C) Differential transmission spectra through an array of $C_{4,z}$ symmetric Au gammadions with 125 nm period placed inside the middle of an empty Fabry-Pérot cavity formed by two 20 nm thick Au mirrors as a function of the cavity thickness. (D) The same as (c) but for an array of gammadions with removed central bar yielding only $C_{2,z}$ symmetry. Note the two orders of magnitude difference in values.

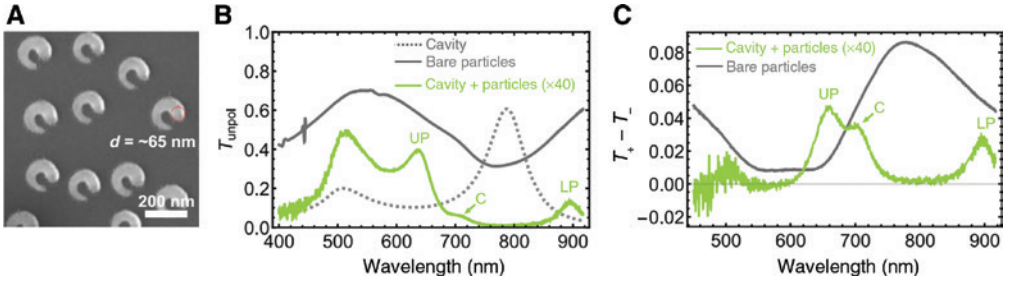

Figure 6: Experiments with chiral hybrid cavity-plasmon system.
(A) SEM image of chiral Au nanocrescents on glass substrate with ~65 nm head diameter, assumed for FDTD simulations. (B) Unpolarized $(T_+ + T_-)/2$ transmission spectra of bare chiral nanocrescents on glass substrate, bare Fabry-Pérot cavity, and that of the coupled cavity-plasmon system. UP and LP label the position of upper and lower cavity-plasmon polaritons, whereas C labels the middle "uncoupled" peak due to in-plane anisotropy of the particles. (C) CD spectra of the same two systems, showing emerging mode splitting in CD of the coupled plasmon-cavity structure.

the CD spectrum of the bare particles (calculated as the differential total transmission $T_+ - T_-$) shows a broad peak around 800 nm, Figure 6C. The observed redshift of the plasmon peak from 700 nm in FDTD simulations to 800 nm in experiment is likely caused by the effect of the glass substrate.

To arrange a coupled system, gold nanocrescents were deposited on top of half-cavity consisting of 20 nm gold film (serving as a bottom mirror) on glass substrate and ~100 nm thick SiO_2 layer, using the same technique as bare nanoparticles. Then, the half-cavity with nanoparticles was completed by depositing 100 nm of PMMA layer, and another 20 nm gold film as a top mirror. The thickness of the FP cavity was ~200 nm to tune the cavity resonance to ~800 nm (the dashed curve in Figure 6B).

An unpolarized transmission spectrum of the coupled system at normal incidence shows the presence of two peaks at around 640 and 900 nm in Figure 6B, unambiguously indicating emergence of the mode splitting due to strong coupling of plasmonic oscillators to the cavity mode [28]. The transmission spectrum also reveals a middle peak at around 700 nm, which likely originates from the nanocrescents anisotropy, as discussed above. Finally, the resulting CD spectra also clearly demonstrate splitting of the initial plasmon CD peak into two hybrid cavity-plasmon modes located at the nearly same wavelengths of 650 and 900 nm, as shown in Figure 6C, thus confirming our theoretical prediction. We stress one more time that the observed asymmetric transmission originates from both chirality and anisotropy of the plasmonic nanostructure. Transmission and CD spectra measured from strongly coupled systems with different geometrical parameters presented in Figure S7 demonstrate qualitatively similar behavior.

The demonstrated effect of CD mode splitting is reminiscent of the CD enhancement from chiral molecules by plasmon resonances demonstrated by Govorov and colleagues [11, 12, 14], with the exception that no CD enhancement has been observed in our system. In their studies, the plasmon resonance of a metallic nanoparticle in the visible range was interacting with the tail of the chiral electronic transition of a molecule at higher energies. The plasmon resonance picks up the tail of the chiral molecule in the visible range and amplifies it due to excitation of the superchiral near fields. This scenario can equally be interpreted as the mode splitting of CD with the uncoupled components being largely detuned in the first place, whereas we achieved the splitting by means of a large coupling constant. In contrast to our observations, in those studies CD enhancement was observed, since the near fields of plasmonic nanocavities allow formation of superchiral field distributions as opposed to planar isotropic cavities. Nevertheless, our study has indicated that strongly red-detuned Fabry-Pérot microcavities could in principle also pick up the tail of the chiral molecule resonance (see e.g. Figure 1B), which could lead to emergence of a measurable CD peak in the visible range. However, the magnitude of this peak will be somewhat reduced in comparison to the otherwise slowly varying free space CD signal, since most relevant chiral molecules absorb in the UV range. The usefulness of this approach for practical chiral sensing applications, however, remains to be verified.

5 Conclusion

In conclusion, we have demonstrated that generalized mode splitting can be induced in circular dichroism spectra of a chiral system, such as a molecule or a nanoparticle scatterer, by strong coupling to an achiral optical cavity. The resulting polariton modes inherit the chiral nature of its constituents and exhibit the mode splitting – the hallmark of the strong coupling regime – not only in transmission and absorption, but also in their CD spectra, thus allowing to split dichroic response of the system. At the same time, the use of planar cavities for strong coupling imposes fundamental limitations on the enhancement of CD spectra, which originate from the nature of CP standing waves. The overall decrease of CD magnitude from the coupled system makes this approach less valuable for sensing applications. Nevertheless, we have suggested possible ways to overcome this limitation. The predicted effect was observed in a proof-of-principle experiment involving chiral plasmonic nanoparticles strongly coupled to a Fabry-Pérot cavity.

Acknowledgements: We thank Constantin Simovski for helpful discussion. The work was supported by Swedish Research Council Infrastructure grant and the Knut and Alice Wallenberg Foundation.

Appendix A: Transfer-matrix method

We have adopted the formalism of *T*-matrix, describing propagation of plane waves in a planar multilayer structure [39]. The multilayer system is broken down into two types of primitive elements: homogeneous slabs and heterogeneous interfaces between two different media. For each element, the respective *T*-matrix connects complex amplitudes of forward- and backward propagating waves on the left and right sides of the element:

$$\begin{pmatrix} c \\ d \end{pmatrix} = \begin{pmatrix} T_{11} & T_{12} \\ T_{21} & T_{22} \end{pmatrix} \begin{pmatrix} a \\ b \end{pmatrix},$$

where a and b are amplitudes of the forward and backward wave on the left side, and c and d are those on the right side, respectively. In an isotropic chiral medium the propagating eigenmodes are circularly polarized plane waves [29]; furthermore, the rotation direction of CP waves is preserved (although the handedness reverses upon reflection). Therefore, the T-matrix will relate the amplitudes of waves having the same rotation direction.

For a fixed incident circular polarization, the T-matrix of a homogeneous layer of thickness L is diagonal (since there is no reflection within the layer) and reads $T_i = \begin{pmatrix} e^{ik_{i,+}L} & 0 \\ 0 & e^{-ik_{i,-}L} \end{pmatrix}$, where $k_{i,+}$ and $k_{i,-}$ are the wave vectors of forward and backward propagating waves in i-th layer, respectively. For a bi-isotropic reciprocal chiral medium the wave vectors read [29] $k_{i,\pm} = \frac{\omega}{c}(\sqrt{\varepsilon_i \mu_i} \pm \kappa_i)$.

The T-matrix for an interface T_{ij} can be derived from the corresponding scattering matrix that relates outgoing waves to the incoming ones: $\begin{pmatrix} b \\ c \end{pmatrix} = \begin{pmatrix} r_{ij} & t_{ji} \\ t_{ij} & r_{ji} \end{pmatrix} \begin{pmatrix} a \\ d \end{pmatrix}$, where r_{ij} and t_{ij} are the complex reflection and transmission electric field coefficients for incidence from medium i toward medium j. For an interface between two bi-isotropic reciprocal chiral media, these coefficients read [29]: $r_{ij} = (\eta_{i,+}^{-1} - \eta_{j,+}^{-1})/(\eta_{i,-}^{-1} + \eta_{j,+}^{-1})$, $t_{ij} = 1 + r_{ij}$, where $\eta_{i,\pm} = \sqrt{\mu_i / \varepsilon_i}$ are characteristic impedances of the two media, and + and – denote forward and backward propagating waves (with respect to the wave incident onto the interface). One can observe that $\eta_{i,\pm}$ are independent of the propagation direction. Resolving the interface scattering matrix with respect to the amplitudes of the waves on the right side c and d, we find $\begin{pmatrix} c \\ d \end{pmatrix} = \frac{1}{t_{ji}} \begin{pmatrix} t_{ij}t_{ji} - r_{ij}r_{ji} & r_{ji} \\ -r_{ij} & 1 \end{pmatrix} \begin{pmatrix} a \\ b \end{pmatrix}$.

The resulting T-matrix of the entire system T_Σ is found as the product of T-matrices of consecutive interfaces and layers: $T_\Sigma = T_{n-1,n} \cdot T_n \cdot \ldots \cdot T_2 \cdot T_{12}$. Finally, resolving this matrix with respect to b and c and letting $d = 0$ (no incidence from the right side), we found the desired reflection and transmission coefficients:

$$t = T_{11}^{\Sigma} - \frac{T_{12}^{\Sigma} T_{21}^{\Sigma}}{T_{22}^{\Sigma}}, \quad r = -\frac{T_{21}^{\Sigma}}{T_{22}^{\Sigma}}.$$

The total T-matrix for the opposite incident circular polarization can simply be obtained by flipping $\kappa_i \to -\kappa_i$ and performing the same procedure.

Appendix B: FDTD simulations

Numerical simulations of the electromagnetic response of Au nanocrescents were performed using the finite-difference time-domain (FDTD) method using commercial software (Lumerical, Canada). A single nanoscrescent was simulated inside a 600 nm × 600 nm × 600 nm simulation region with 12 layers thick PML and with a total field/scattered field (TFSF) source. Transmission spectra and Jones matrix elements of uncoupled and coupled cavities were obtained using a normal incidence plane wave source and in-plane periodic boundary conditions. The mesh accuracy parameter was set to 8 with a fixed mesh step of 2 nm around the nanocrescent; a simulations time of 600 fs was used with the auto-shutoff parameter of 10^{-6} to ensure decay of residual oscillating field for calculating the differential transmission and scattering.

Appendix C: Multipole decomposition

The Cartesian electric, toroidal, magnetic, and magnetic toroidal dipole moments of a single nanocrescent were calculated using the standard expansion formulas [40]:

$$\mathbf{P} = \varepsilon_0(\varepsilon - 1)\int \mathbf{E} dV,$$

$$\mathbf{T} = \frac{k^2}{10}\varepsilon_0(\varepsilon - 1)\int[(\mathbf{r}\cdot\mathbf{E})\mathbf{r} - 2r^2\mathbf{E}]dV,$$

$$\mathbf{M} = -i\frac{\omega}{2}\varepsilon_0(\varepsilon - 1)\int \mathbf{r}\times\mathbf{E} dV,$$

$$\mathbf{M}_t = i\frac{k^2\omega}{20}\varepsilon_0(\varepsilon - 1)\int r^2\mathbf{r}\times\mathbf{E} dV.$$

The corresponding electric and magneto-electric dipole polarizabilities (their x-components) in μm^3 were then calculated as $\alpha_{ee} = (P_x + T_x)/(\varepsilon_0 E_{\text{inc}})$ and $\alpha_{em} = (M_x + M_{t,x})/(\varepsilon_0 E_{\text{inc}})$ with E_{inc} being the electric field of the incident plane wave.

Appendix D: Sample fabrication

Glass substrates were cleaned with hot acetone and isopropanol, respectively, to remove impurities. To fabricate coupled system, first, 20 nm of gold thin film for bottom

mirror was prepared using an e-beam evaporator. Then, ~100–107.5 nm of SiO_2 layers were deposited using STS plasma-enhanced chemical vapor deposition (PECVD) at 300°C, to form half-cavities. Later, chiral nanoparticles were deposited on top of the half-cavities or directly on bare glass substrates, to fabricate coupled systems or reference bare particles, respectively.

Chiral nanoparticles were fabricated using hole-colloidal lithography technique (HCL), using techniques described in [34, 36]. Firstly, ~240 nm thick poly(methyl methacrylate) (PMMA) layer was spin coated on the substrates (half-cavities or bare glass), baked at 180°C for 10 min, and then functionalized with polydiallyldimethylammonium chloride (PDDA, 0.2%) aqueous solution for 30 s. Subsequently, 80 or 100 nm of polystyrene (PS) beads were applied on the functionalized-substrates. After 3 min, the samples were rinsed gently with water and dried with nitrogen. Then, 10 nm of gold thin film was evaporated, and PS beads with 10 nm gold caps were removed with tape-stripping. Later, the samples were dry etched using oxygen plasma (4 min, 50 W, 250 mTorr) to form hole-mask. For the deposition of chiral gold nanoparticles, 120 nm of gold was evaporated with rate of 2 Å/s at substrate tilt angle of 13° while rotating the substrate at a constant speed over total angle of 270°, followed by removal of PMMA resists with hot acetone and rinsed with isopropanol. Afterwards, the nanoparticles were annealed at 250°C for 10 min to improve the crystallinity of the particles.

For the coupled systems, PMMA layer with same thicknesses as the bottom SiO_2 half-cavity was spin coated and annealed at 180°C for 10 min, followed by evaporation of 20 nm gold thin film as a top mirror to complete the cavity. Bare FP cavity was prepared with same procedures as coupled system, except of the nanoparticles deposition.

Appendix E: Optical characterization

Polarization-resolved transmission spectra were measured using circularly polarized white light from a halogen light as a broadband illumination. Broadband right or left polarized light were obtained by transmitting the white light through a polarizer misaligned of either +45° or −45° with respect to a Fresnel rhomb, respectively [34]. Transmission spectra of the samples were collected using a fiber coupled spectrometer (BWTek). Reference spectrum was taken with bare glass substrate under same measurement condition.

References

[1] Barron LD. Molecular light scattering and optical activity. Cambridge, Cambridge University Press, 2009.
[2] Craig DP, Thirunamachandran T. Molecular quantum electrodynamics : an introduction to radiation-molecule interactions. New York, Dover Publications, 1998.
[3] Leitereg TJ, Guadagni DG, Harris J, Mon TR, Teranishi R. Chemical and sensory data supporting the difference between the odors of the enantiomeric carvones. J Agric Food Chem 1971;19:785–7.
[4] Fasman GD. Circular dichroism and the conformational analysis of biomolecules. New York, Springer, 2011.
[5] Inoue Y, Ramamurthy V. Chiral photochemistry. New York, Marcel Dekker, 2004.
[6] Chhabra N, Aseri ML, Padmanabhan D. A review of drug isomerism and its significance. Int J Appl Basic Med Res 2013;3:16–8.
[7] Hendry E, Carpy T, Johnston J, et al. Ultrasensitive detection and characterization of biomolecules using superchiral fields. Nat Nanotechnol 2010;5:783–7.
[8] Zhang H, Zheng X, Kwok RTK, et al. In situ monitoring of molecular aggregation using circular dichroism. Nat Commun 2018;9:4961.
[9] Tang Y, Cohen AE. Enhanced enantioselectivity in excitation of chiral molecules by superchiral light. Science 2011;332:333–6.
[10] Yang N, Tang Y, Cohen AE. Spectroscopy in sculpted fields. Nano Today 2009;4:269–79.
[11] Govorov AO, Fan Z, Hernandez P, Slocik JM, Naik RR. Theory of circular dichroism of nanomaterials comprising chiral molecules and nanocrystals: plasmon enhancement, dipole interactions, and dielectric effects. Nano Lett 2010;10:1374–82.
[12] Slocik JM, Govorov AO, Naik RR. Plasmonic circular dichroism of peptide-functionalized gold nanoparticles. Nano Lett 2011;11:701–5.
[13] Kneer LM, Roller E-M, Besteiro LV, Schreiber R, Govorov AO, Liedl T. Circular dichroism of chiral molecules in DNA-assembled plasmonic hotspots. ACS Nano 2018;12:9110–5.
[14] Zhang H, Govorov AO. Giant circular dichroism of a molecule in a region of strong plasmon resonances between two neighboring gold nanocrystals. Phys Rev B 2013;87:75410.
[15] Davis TJ, Gómez DE. Interaction of localized surface plasmons with chiral molecules. Phys Rev B 2014;90:235424.
[16] Maoz BM, Chaikin Y, Tesler AB, et al. Amplification of chiroptical activity of chiral biomolecules by surface plasmons. Nano Lett 2013;13:1203–9.
[17] Lu F, Tian Y, Liu M, et al. Discrete nanocubes as plasmonic reporters of molecular chirality. Nano Lett 2013;13:3145–51.
[18] García-Guirado J, Svedendahl M, Puigdollers J, Quidant R. Enantiomer-selective molecular sensing using racemic nanoplasmonic arrays. Nano Lett 2018;18:6279–85.
[19] Lipkin DM. Existence of a new conservation law in electromagnetic theory. J Math Phys 1964;5:696–700.
[20] Meinzer N, Hendry E, Barnes WL. Probing the chiral nature of electromagnetic fields surrounding plasmonic nanostructures. Phys Rev B 2013;88:041407.
[21] Yang N, Cohen AE. Local geometry of electromagnetic fields and its role in molecular multipole transitions. J Phys Chem B 2011;115:5304–11.
[22] Tang Y, Cohen AE. Optical chirality and its interaction with matter. Phys Rev Lett 2010;104:163901.

[23] Khitrova G, Gibbs HM, Kira M, Koch SW, Scherer A. Vacuum Rabi splitting in semiconductors. Nat Phys 2006;2: 81–90.
[24] Törma P, Barnes WL. Strong coupling between surface plasmon polaritons and emitters: a review. Rep Prog Phys 2015;78:13901.
[25] Baranov DG, Wersäll M, Cuadra J, Antosiewicz TJ, Shegai T. Novel nanostructures and materials for strong light–matter interactions. ACS Photonics 2018;5:24–42.
[26] Ameling R, Giessen H. Microcavity plasmonics: strong coupling of photonic cavities and plasmons. Laser Photonics Rev 2013;7:141–69.
[27] Ameling R, Giessen H. Cavity plasmonics: large normal mode splitting of electric and magnetic particle plasmons induced by a photonic microcavity. Nano Lett 2010;10:4394–8.
[28] Bisht A, Cuadra J, Wersäll M, Canales A, Antosiewicz TJ, Shegai T. Collective strong light-matter coupling in hierarchical microcavity-plasmon-exciton systems. Nano Lett 2019;19:189–96.
[29] Lindell I, Sihvola A, Tretyakov S, Vitanen A. Electromagnetic waves in chiral and bi-isotropic media. Artech House, 2018.
[30] Bai B, Svirko Y, Turunen J, Vallius T. Optical activity in planar chiral metamaterials: theoretical study. Phys Rev A 2007;76:023811.
[31] Graf F, Feis J, Garcia-Santiago X, Wegener M, Rockstuhl C, Fernandez-Corbaton I. Achiral, helicity preserving, and resonant structures for enhanced sensing of chiral molecules. ACS Photonics 2019;6:482–91.
[32] Plum E, Zheludev NI. Chiral mirrors. Appl Phys Lett 2015;106:221901.
[33] Feis J, Beutel D, Köpfler J, et al. Helicity-preserving optical cavity modes for enhanced sensing of chiral molecules. 2019. Available at: https://arxiv.org/abs/1907.05207.
[34] Verre R, Shao L, Odebo Länk N, et al. Metasurfaces and colloidal suspensions composed of 3D chiral Si nanoresonators. Adv. Mater. 2017;29:1701352.
[35] Frank B, Yin X, Schäferling M, et al. Large-area 3d chiral plasmonic structures. ACS Nano 2013;7:6321–9.
[36] Fang Y, Verre R, Shao L, Nordlander P, Käll M. Hot electron generation and cathodoluminescence nanoscopy of chiral split ring resonators. Nano Lett 2016;16:5183–90.
[37] Goerlitzer ESA, Mohammadi R, Nechayev S, Banzer P, Vogel N. Large-area 3D plasmonic crescents with tunable chirality. Adv Opt Mater 2019;1801770:1–9.
[38] Menzel C, Rockstuhl C, Lederer F. Advanced jones calculus for the classification of periodic metamaterials. Phys Rev A 2010;82:053811.
[39] Haus H. Waves and fields in optoelectronics. Prentice Hall: Englewood Cliffs, 1984.
[40] Fernandez-Corbaton I, Nanz S, Alaee R, Rockstuhl C. Exact dipolar moments of a localized electric current distribution. Opt Express 2015;23:33044.

Supplementary Material: The online version of this article offers supplementary material (https://doi.org/10.1515/nanoph-2019-0372).